Article

Quasi-equilibrium growth of inch-scale single-crystal monolayer α-In$_2$Se$_3$ on fluor-phlogopite

Kunpeng Si[1,9], Yifan Zhao[2,3,9], Peng Zhang [1] ✉, Xingguo Wang[1], Qianqian He[1,4], Juntian Wei[1], Bixuan Li[1], Yongxi Wang[1], Aiping Cao[5], Zhigao Hu [5], Peizhe Tang [1,6] ✉, Feng Ding [2,3] ✉ & Yongji Gong [1,7,8] ✉

Epitaxial growth of two-dimensional (2D) materials with uniform orientation has been previously realized by introducing a small binding energy difference between the two locally most stable orientations. However, this small energy difference can be easily disturbed by uncontrollable dynamics during the growth process, limiting its practical applications. Herein, we propose a quasi-equilibrium growth (QEG) strategy to synthesize inch-scale monolayer α-In$_2$Se$_3$ single crystals, a semiconductor with ferroelectric properties, on fluor-phlogopite substrates. The QEG facilitates the discrimination of small differences in binding energy between the two locally most stable orientations, realizing robust single-orientation epitaxy within a broad growth window. Thus, single-crystal α-In$_2$Se$_3$ film can be epitaxially grown on fluor-phlogopite, the cleavage surface atomic layer of which has the same 3-fold rotational symmetry with α-In$_2$Se$_3$. The resulting crystalline quality enables high electron mobility up to 117.2 cm^2 V^{-1} s^{-1} in α-In$_2$Se$_3$ ferroelectric field-effect transistors, exhibiting reliable nonvolatile memory performance with long retention time and robust cycling endurance. In brief, the developed QEG method provides a route for preparing larger-area single-crystal 2D materials and a promising opportunity for applications of 2D ferroelectric devices and nanoelectronics.

Two-dimensional (2D) materials, such as MoS$_2$ and In$_2$Se$_3$, hold significant importance for the semiconductor industry because of their atomic thickness[1,2], excellent physical properties[3,4], and processing compatibility[5,6]. In the application of 2D materials in electronics, the device performance is significantly affected by grain boundaries and crystallographic defects[7]. Naturally, these materials within a single crystal domain can strongly improve the performance and consistency of semiconducting devices, so the growth of large-area single crystals of 2D materials has been urgent[8].

At present, two main methods are used for the growth of single-crystal 2D materials: the phase transformation and the epitaxial growth on single-crystal substrates. Phase transformation is to transform a large area of 2D polycrystalline film into single-crystal samples gradually by introducing a single-crystal seed, which has been applied to

[1]School of Materials Science and Engineering, Beihang University, Beijing, P. R. China. [2]Institute of Technology for Carbon Neutrality, Shenzhen Institute of Advanced Technology, Chinese Academy of Sciences, Shenzhen, China. [3]Faculty of Materials Science and Energy Engineer, Shenzhen University of Advanced Technology, Shenzhen, China. [4]The Analysis & Testing Center, Beihang University, Beijing, P. R. China. [5]Technical Center for Multifunctional Magneto Optical Spectroscopy (Shanghai), Department of Physics, School of Physics and Electronic Science, East China Normal University, Shanghai, P. R. China. [6]Center for Free-Electron Laser Science, Max Planck Institute for the Structure and Dynamics of Matter, Hamburg, Germany. [7]Tianmushan Laboratory Xixi Octagon City, Hangzhou, P. R. China. [8]Center for Micro-Nano Innovation of Beihang University, Beijing, P. R. China. [9]These authors contributed equally: Kunpeng Si, Yifan Zhao. ✉e-mail: zhangpeng567@buaa.edu.cn; peizhet@buaa.edu.cn; f.ding@siat.ac.cn; yongjigong@buaa.edu.cn

some specific 2D materials[9]. In epitaxial growth, a few types of substrates with surface atomic layer in 3-fold rotational symmetry or 6-fold rotational symmetry with specific steps (such as Cu, Al_2O_3, etc.)[8,10–12] are used for the growth of single-crystal 2D materials. In this case, when 2D materials with 3-fold rotational symmetry (such as MoS_2 and h-BN) are grown on a 3-fold substrate, depending on the influence of exposed atoms on the substrate surface, two locally most stable states (with a 60° difference) sometimes occur, and the binding energy difference between these two states is very small. However, this small energy difference can be easily disturbed by the uncontrollable dynamics in a typical chemical vapor deposition (CVD) process, such as uneven gas flow and inhomogeneous vapor distribution, resulting in orientation inconsistency. Thus, some new strategies are highly desired to make this small binding energy difference repeatedly and reliably induce orientated growth of 2D materials.

To address this problem, we devise a quasi-equilibrium growth (QEG) method, using α-In_2Se_3 as an example, to synthesize inch-scale single-crystal monolayer films. Gaining attention as a layered ferroelectric semiconductor, α-In_2Se_3 is notable for its room-temperature ferroelectricity[13], even at the 2D limit, making it a promising candidate for next-generation electronic devices, such as non-volatile memory (NVM)[14,15], ferroelectric field-effect transistors (Fe-FETs)[16,17], and neuromorphic computing[18]. Fluor-phlogopite is selected as the substrate because the cleavage atomic surface shares the same 3-fold rotational symmetry[19] with α-In_2Se_3, promoting uniform orientations for α-In_2Se_3 islands. Our approach utilizes semi-closed environments, small source-substrate distance, and the liquid intermediate state to realize QEG, ensuring that the small energy difference is not disturbed by the dynamic process, achieving robust growth of spliced single-crystal film within a large growth window. This discovery is consistent with results from our first-principles calculations, suggesting that the mono-orientational α-In_2Se_3 monolayers can be achieved by the epitaxial growth on fluor-phlogopite. By constructing Fe-FETs using α-In_2Se_3 as the channel material and gate respectively, we demonstrate remarkable memory performance in all types of devices, such as large hysteresis windows, long retention time, and robust cycling endurance. Our approach paves the way for the industrial integration of 2D ferroelectric materials in the development of next-generation electronic devices.

Results and discussion
### QEG of α-In_2Se_3 films

Large-scale monolayer α-In_2Se_3 films are synthesized using QEG (methods for details). The whole experiment process is divided into three steps: evaporation, crystallization, and film formation. In the evaporation step, the powder mixture vaporized in a semi-enclosed environment with the temperature increased. The fluor-phlogopite is placed above, and close (<1 mm) to the mixed powders of α-In_2Se_3 and KI (Fig. 1a). A pretty low concentration of KI is enough to facilitate the evaporation of In_2Se_3 (see "Methods" section for details). Due to the decreased melting temperature of In_2Se_3 with the existence of KI[20], the resulting gaseous mixture first liquefies on the fluor-phlogopite surface in the form of tiny droplets. During this step, temperature is the critical factor that determines the size of the droplets. A specific mass ratio ($m(\alpha$-$In_2Se_3)$:$m(KI) = 60$:1) is chosen to verify the influence of temperature. Too high temperature (> 760 °C) will lead to excessively large droplets deposited on fluor-phlogopite surface. Under the competition between the interfacial free energies of droplet/sample and droplet/substrate interface[21], droplets slide on the substrate surface (Fig. 1b, inset). This results in the formation of monolayer or few-layer α-In_2Se_3 ribbons with irregular shape along the sliding path (Fig. 1b) and random orientation. Lower growth temperature (720–760 °C) could develop tiny clusters into triangular or hexagonal samples with uniform orientation. By rapidly cooling the furnace during the evaporation step, the droplets can quickly crystallize and

then be characterized (Supplementary Fig. 1, 2). The sizes of particles formed at different temperatures are counted in Fig. 1e, which gives convincing evidence. In addition, energy dispersive spectroscopy (EDS) proves that the reaction intermediate is mainly composed of In_2Se_3 (Supplementary Fig. 2a). In contrast, samples grown from the precursor powders without KI possess large thickness (Supplementary Fig. 3) without liquid feature, indicating vapor deposition mechanism. Therefore, the temperature determines the way and shape of the sample growth, which needs to be controlled properly to ensure the stability of the evaporation and growth process.

The second step is crystallization, which includes nucleation and growth. With the desired reaction intermediate discussed above, controllable nucleation will be obtained. Then, the tiny clusters move around the surface of substrate and formed flakes, and then captured by the dangling bounds at the edge of α-In_2Se_3 to propagate. Subsequently, the α-In_2Se_3 flakes continue to grow and merge together, forming a smooth and uniform film (Fig. 1c, d). To verify the robustness of this method, we performed five successive experiments to fabricate films on a centimeter scale, which elucidates the high reproducibility in the growth method reported here (Fig. 1f). The homogeneous color in optical photographs indicates the uniform thickness. Extra experiments, employing distinct mass ratios of precursors and varying temperatures, are stopped before film formation to observe the grain size and shape (Supplementary Fig. 4), which are summarized in Supplementary Table 1. By merely extending the growth time, homogeneous films can be consistently obtained with different growth conditions. Our findings reveal that monolayer single-crystal α-In_2Se_3 films can be successfully realized over a broad temperature range, spanning from 700 °C to 800 °C, and varied mass ratios of precursors from 30:1 to 90:1 (Fig. 1g), which demonstrates the high tolerance for preparation conditions. Notably, the lateral size of single α-In_2Se_3 flake can reach 1201 μm (Inset of Fig. 1g) through meticulous control of the temperature at 760 °C and a precursors ratio of 60:1. Additionally, we varied the substrates, solvents, and source-substrate distances to explore a broader range of experimental conditions. These changes tend to deviate the growth process from equilibrium, making it challenging to ensure film uniformity (detailed discussions can be found in the Mechanism section and Supplementary Figs. 5–9).

Mechanism of single-crystal film growth

The ability to splice nano flakes into single-crystal film is due to the lattice symmetry match relationship between substrate and sample[12]. On a substrate, a high symmetric direction of a 2D material aligning along a high symmetric direction of the substrate generally corresponds to a minimum formation energy[22]. Based on the epitaxial principle of 2D materials growth, it has been proved that if the symmetric group of a 2D material possesses all the symmetric operations of the substrate, it is possible to grow parallel aligned 2D materials on the substrate[22]. Therefore, the selection of the proper substrate plays a crucial role in the growth of single-crystal α-In_2Se_3. We choose the fluor-phlogopite, which is atomic flat and highly stable, as the substrate. Such substrate is suitable for the growth of atomically thin layers of many materials[19]. As depicted in Fig. 2a, we can see that the hexagons of the fluor-phlogopite surface are distorted, and the distortion has lowered the symmetry of the surface from 6-fold to 3-fold. Fig 2c shows a 0° and 60° rotated fluor-phlogopite surface and it can be clearly seen that the positions of some oxygen atoms were changed by to 60° rotational operation, which means that the substrate does not own a 60° rotational symmetric operation. The terminated fluor-phlogopite surface possesses a 3-fold rotational symmetry (see details in Fig. 2a and Supplementary Fig. 10), which is same to that of the α-In_2Se_3 ($R\bar{3}m$). Besides, in the ab plane, the lattice constant of In_2Se_3 samples is 4.0260 Å, while the surface atoms of fluor-phlogopite have a lattice constant of 9.2123 Å. As shown in Supplementary Fig. 11, the 7 × 7 In_2Se_3 supercell (7 × 4.0260 = 28.1820 Å) is commensurate with
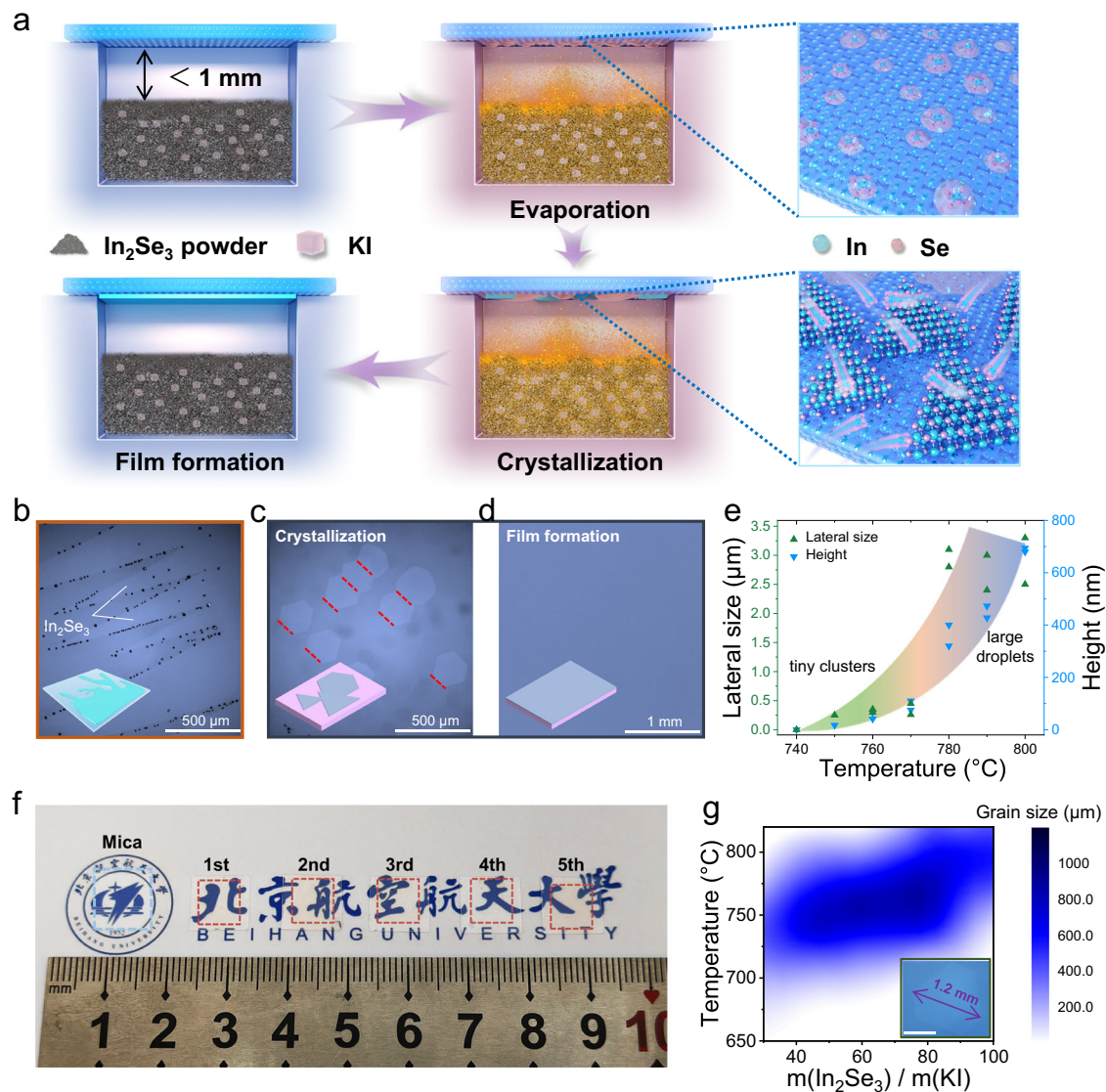
Fig. 1 | Large-area synthesis of α-In$_2$Se$_3$ films. a Schematic of quasi-equilibrium growth (QEG) method of α-In$_2$Se$_3$ films. Step 1: evaporation. Zoom-in schematic illustrates the adherence of tiny clusters on the substrate at this step. Step 2: crystallization. Zoom-in schematic illustrates the bonding of In$_2$Se$_3$ molecules at dangling bonds along the edges of the sample at this step. Step 3: film formation. **b** The sample of irregular shape formed by droplets sliding (KI and α-In$_2$Se$_3$). Inset: schematic of the droplet slip process. **c** Optical images of α-In$_2$Se$_3$ flakes during the crystallization process. Crystal orientation was labeled by red dash lines. **d** Optical images of α-In$_2$Se$_3$ film. Inset: Schematic of the growth process. **e** Temperature dependence of Lateral size and height of droplets at $m(\alpha$-In$_2$Se$_3$): m(KI) = 60:1. The shaded area illustrates the trend of particle size variation with temperature. **f** Photograph of centimeter-scale α-In$_2$Se$_3$ films (right, red dash line) obtained through five consecutive experiments and pristine fluor-phlogopite (left, blue dash line). **g** Crystal size of individual α-In$_2$Se$_3$, which will splice into monolayer films, at different temperature and mass ratio of precursors. Inset: single crystal with lateral size of 1.2 mm. Scale bar: 0.5 mm.
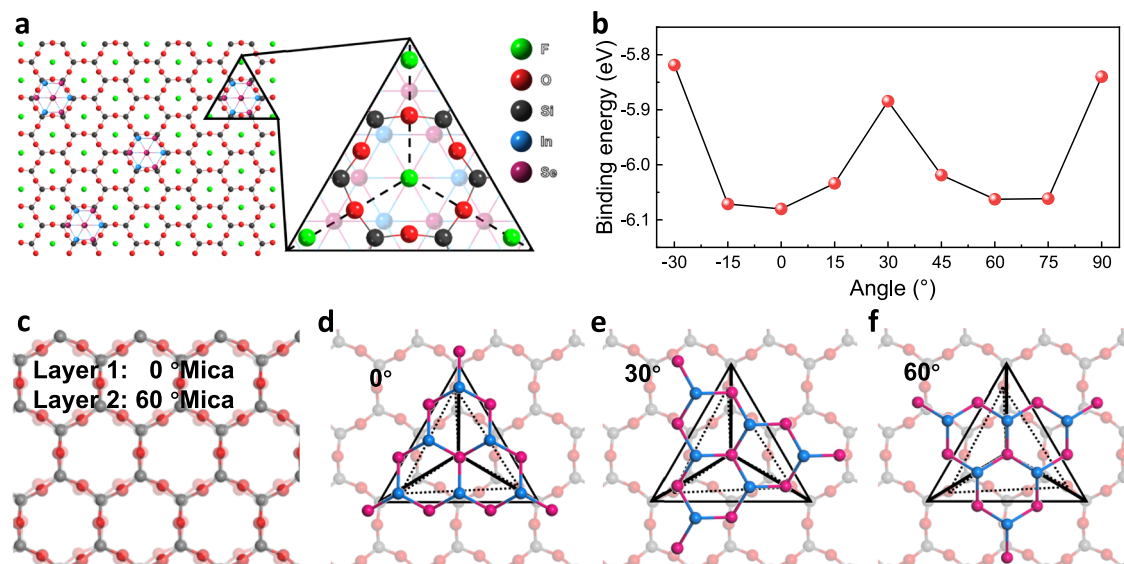
the 3×3 surface atoms of the fluor-phlogopite supercell ($3 \times 9.2123 = 27.6369$ Å) with a 1.9% mismatch. This slight mismatch is tolerable in epitaxial growth processes. Therefore, the formation of parallel α-In$_2$Se$_3$ islands is possible[22].

Our theoretical calculations support the arguments discussed above. A 3-fold rotational symmetric α-In$_2$Se$_3$ flake was placed on the fluor-phlogopite surface along different directions. As illustrated in Fig. 2b, the α-In$_2$Se$_3$ flake attains its lowest binding energy state when the alignment angle between α-In$_2$Se$_3$ and substrate is 0°, which corresponds a high symmetric direction of the system (Fig. 2d). At 60° alignment angle (Fig. 2f), the binding energy is another local minimum which is a slight larger than the global minimum. The very small formation energy difference between α-In$_2$Se$_3$ islands along 0° and 60° explains that a mild environment without obvious disturbance is required to grow α-In$_2$Se$_3$ flakes within parallel orientations.

In this system, the distance between precursors and substrate is <1 mm and the precursor boat is fully covered by the substrate, creating a semi-closed environment. This helps to minimize fluctuations in precursor concentration and nucleation density. It also prevents the disturbance of gas flow (Fig. 1c). Liquid intermediate can further resist gas flow disturbance, resulting in superior stability for nucleation compared to the vapor-solid process.

More importantly, the semi-closed environment, small source-substrate distance (similar temperature), and the liquid intermediate state (small clusters) collectively establish the QEG. The crystalline growth takes place under quasi-equilibrium conditions, resulting in quasi-equilibrium state among powder, vapor, and products (1).

$$Powders \rightleftharpoons Vapor \rightleftharpoons 2D\,materials \qquad (1)$$

Fig. 2 | Atomic structures of α-In₂Se₃ flake and fluor-phlogopite substrate. **a** Atomic structure of fluor-phlogopite (001) substrate with α-In₂Se₃ seedings. **b** The binding energy of a α-In₂Se₃ flake, with the C₃ᵥ symmetry, on the fluor-phlogopite surface as a function of the rotation angle, where the binding energy at 0° rotation angle is the global minimum and that at 60° rotation angle is a local minimum. **c** Overlap diagram between the fluor-phlogopite surface structure rotated by 60° and the non-rotated fluor-phlogopite surface structure, from which we can see that the fluor-phlogopite surface does not have a 6-fold symmetry axis. **d**–**f** The atomic structures of the α-In₂Se₃ flake on the fluor-phlogopite surface with rotated angles of 0°, 30°, and 60°, respectively, in which only the first layer of fluor-phlogopite and the bottom layer of α-In₂Se₃ flakes in contact with the substrate are displayed. To clearly mark the 3-fold symmetry of the fluor-phlogopite surface, the silicon atoms and oxygen atoms on fluor-phlogopite surface were connected by solid lines and dotted line triangles, respectively.

Firstly, the following derivation is used to explain why the growth here is considered as quasi-equilibrium process. The relationship between partial vapor pressure and temperature can be described using the Clapeyron Eq. (2):

$$\frac{dP}{dT} = \frac{\triangle H}{T \triangle V} \tag{2}$$

where $\frac{dP}{dT}$ is the rate of change of pressure with respect to temperature along the coexistence curve; $\triangle H$ is the enthalpy change associated with the phase transition; T is the temperature; $\triangle V$ is the change in volume associated with the phase transition. Given the abundance of precursor powder in the semi-closed system, it is reasonable to consider that the vapor pressure within the confined space is at equilibrium. Therefore, the growth process can be considered as an isobaric process. The chemical potential difference ($\triangle \mu$) between the product and the precursor can be described using the following Eq. (3):

$$\triangle \mu = \int_{P_0}^{P} \triangle V dP - \int_{T_0}^{T} \frac{\triangle H}{T} dT = \frac{\triangle H}{T} \triangle T \tag{3}$$

where $\triangle T$ is the temperature difference between the product and the precursor powder. The temperature difference between the substrate and the powder is very small ($\triangle T \ll T$) due to the close source-substrate distance. Thus, the $\triangle \mu$ between the product and the precursor is also very small, leading to QEG. This characteristic renders the entire growth process a rigorously thermodynamically controlled characteristic, enabling the differentiation of small binding energy variations for different orientations. Even minute energy differences between the two locally most stable orientations lead to the ultimate epitaxial growth of a single orientation. Thus, single crystals with well-aligned orientation can be synthesized with good repeatability and wide growth window (such as 700–760 °C at $m(\alpha\text{-In}_2\text{Se}_3):m(\text{KI}) = 60:1$). Conversely, in the vapor-phase growth process in open systems, typically occurring far from equilibrium, the growth process is subject to the control of kinetic parameters, significantly enhancing the likelihood of thermodynamic metastable orientation crystallization and impeding the achievement of a single orientation.

In addition, compared to other methods to synthesize single-crystal 2D materials, the size of single 2D materials domain grown by this QEG method can be up to 1201 µm, showing an order of magnitude improvement (Fig. 3a). Finally, same oriented α-In₂Se₃ flakes can stitch together to form a single-crystal film on fluor-phlogopite, resulting in single-crystal film with much decreased spliced interfaces. This gentle approach can be easily extended to wafer-scale samples close to 2 inches (Fig. 3b).

Four characterization methods were adopted to recognize the orientation of α-In₂Se₃ flakes and test whether the as-grown film is single crystalline or not. Convincing results were achieved by using samples with relatively small grain size due to limitations in sample characterization methods. First, we stop the growth process in the crystallization step. Through the optical photographs, an identical orientation could be observed in all small islands of α-In₂Se₃ flakes (Fig. 3c), which is the precondition of single-crystal film formation. The AFM image shows a grain size of approximately 1 µm, which was prepared at 800 °C for 20 s (as shown in Fig. 3c Inset and Supplementary Fig. 12a). Additionally, optical images of samples with a grain size of around 20 µm transferred onto SiO₂/Si, which were prepared at 770 °C for 3 minutes, also depict the same oriented α-In₂Se₃ flakes (as shown in Supplementary Fig. 12b). Next, uniform film (Fig. 3d) was annealed in 10 % H₂/Ar at 400 °C for 30 min to etch holes (Fig. 3e) while the single-crystal characteristics of the sample remain unaffected by annealing[23]. The triangle holes with the same orientation in the film indicate the single-crystal nature. Besides, thin films with grain size of ~50 µm (prepared at 770 °C for 40 min) were prepared for electron backscatter diffraction (EBSD) and transmission electron microscopy (TEM). EBSD was conducted to verify the orientation of the sample over a relatively large area. The uniform color in the grain orientation diagram confirms the single crystalline nature (Fig. 3f Inset). The grain size distribution histogram shows that the samples in the entire scanning area belong to one grain (Fig. 3f). Finally, TEM was used to characterize the crystallization condition of the film. Annular dark-field scanning transmission electron microscopy (ADF-STEM)
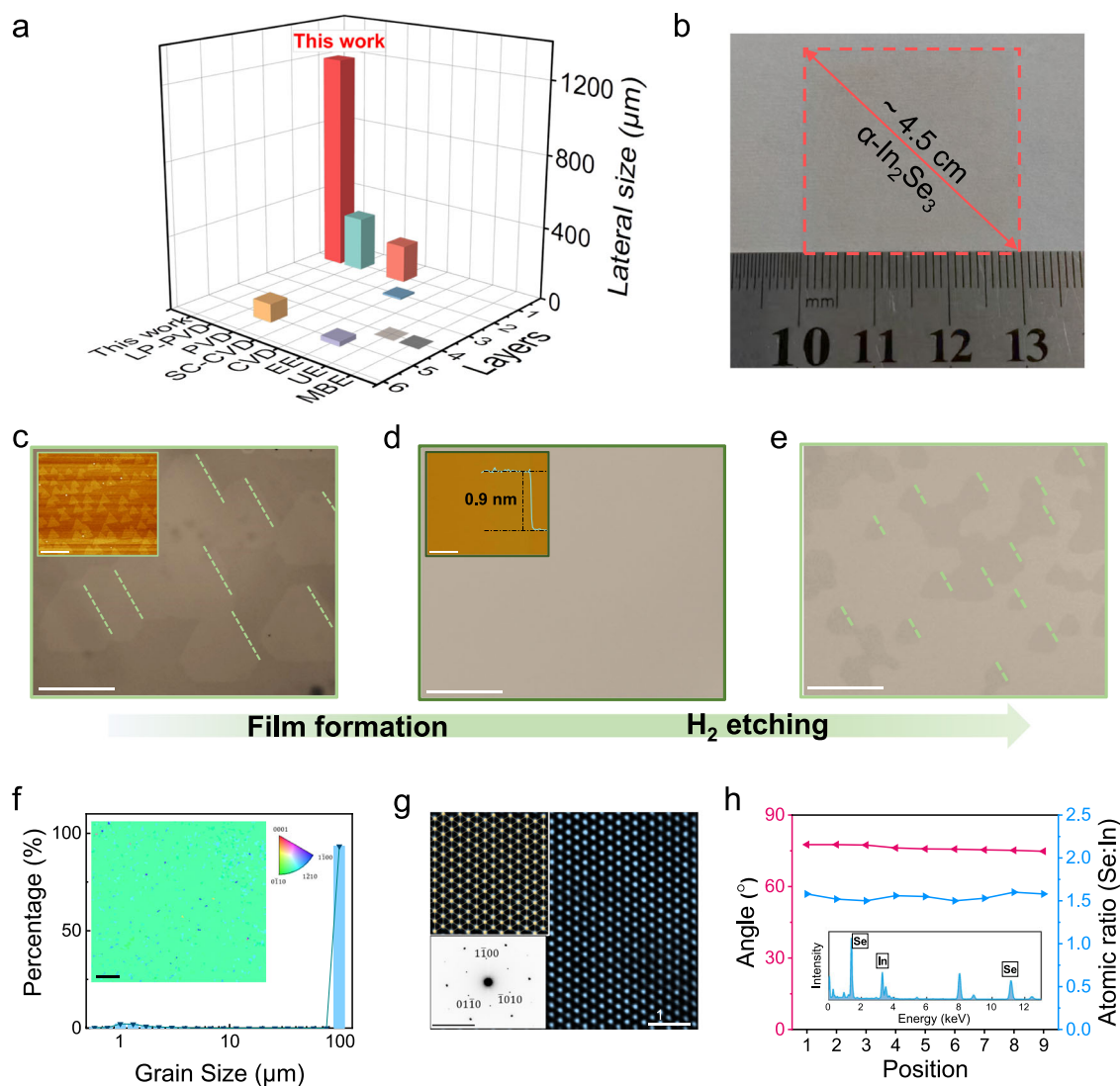
Fig. 3 | Wafer scale α-In₂Se₃ single crystals. a Number of layers and the size of individual samples prepared by QEG (This work), physical vapor deposition (PVD)[29], low-pressure PVD (LP-PVD)[30], chemical vapor deposition (CVD)[31], space-confined CVD (SC-CVD)[24], electrochemical exfoliation (EE)[32], ultrasonic exfoliation (UE)[33], molecular beam epitaxy (MBE)[34]. **b** Photograph of nearly 2-inch α-In₂Se₃ films. **c**−**e** Optical image of α-In₂Se₃ sample during crystallization (**c**), after film formation (**d**), and after H₂ etching (**e**). Inset: atomic force microscopy (AFM) image of grains and uniform film. Scale bar: 2 μm for AFM images and 300 μm for optical images. **f** Grain size distribution counted by electron backscatter diffraction (EBSD). Inset: EBSD inverse pole figure (IPF) mappings. Scale bar: 15 μm. **g** Atomic annular dark-field scanning transmission electron microscopy (ADF-STEM) images of as-synthesized α-In₂Se₃. Inset: Top view of atom structure of α-In₂Se₃ and selected area electron diffraction (SAED) patterns of α-In₂Se₃ (Scale bar: 5 nm⁻¹). **h** Angles, between crystal plane and horizontal position, and atomic ratio collected at 9 different locations corresponding to Supplementary Figs. 14 and 16. Inset: energy dispersive spectroscopy (EDS) of as-grown α-In₂Se₃.

images (Fig. 3g) reveal that the interplanar spacing of the crystal is ~3.5 Å, which corresponds well to the distance of the (1$\bar{1}$00) plane of α-In₂Se₃. Selected area electron diffraction (SAED) and high-resolution atomic images are collected around the junction of two single crystals and exhibited the same orientation and perfect lattice periodicity (Supplementary Fig. 13). The observed atomic positions match well with that in a perfect crystal structure and no obvious defects are observed. SAED (Fig. 3g Inset) demonstrates that the crystal exhibits a 6-fold symmetry diffraction pattern. SAED from adjacent 9 TEM grid holes in a line, over 1 mm, on the TEM grid show similar angles with a deviation of only 2.8 degrees (Fig. 3h and Supplementary Fig. 14), which is the convincing evidence for a single crystal. The negligible deviation can mainly be attributed to the distortion generated during the transfer process.

Our samples have a high crystal quality within a single crystal form. High-resolution XRD shows typical single-crystal diffraction peaks of α-In₂Se₃ (Supplementary Fig. 15). The EDS analysis (Fig. 3h Inset and Supplementary Fig. 16) confirms that there are no K or I elements in as-grown samples. The distinct peaks of K and I element are also not detected in X-ray photoelectron spectroscopy (XPS) and Auger electron spectroscopy (AES) (Supplementary Figs. 17, 18). This is the key factor indicating the high quality of our samples. Furthermore, the uniform distribution of elements in as-grown samples with Se/In ratio of approximately 3:2 was confirmed using STEM atomic-resolved EDS mapping (Fig. 3f and Supplementary Fig. 19). The Low wave-number Raman spectrum at nine randomly chosen positions shows characteristic peaks of α phase In₂Se₃ and Raman mapping at 102 cm⁻¹ indicates the uniformity of α-In₂Se₃ film (Supplementary Figs. 20 and 21). The thickness of as-grown films is determined to be ~0.9 nm by atomic force microscopy (AFM) (Fig. 3d inset). The morphology of AFM demonstrates atomic flatness without a second layer or seeds on the top surface. Nine uniformly dispersed locations on the prepared film are selected to characterize its thickness (Supplementary Fig. 22), which shows uniform monolayer characteristics.
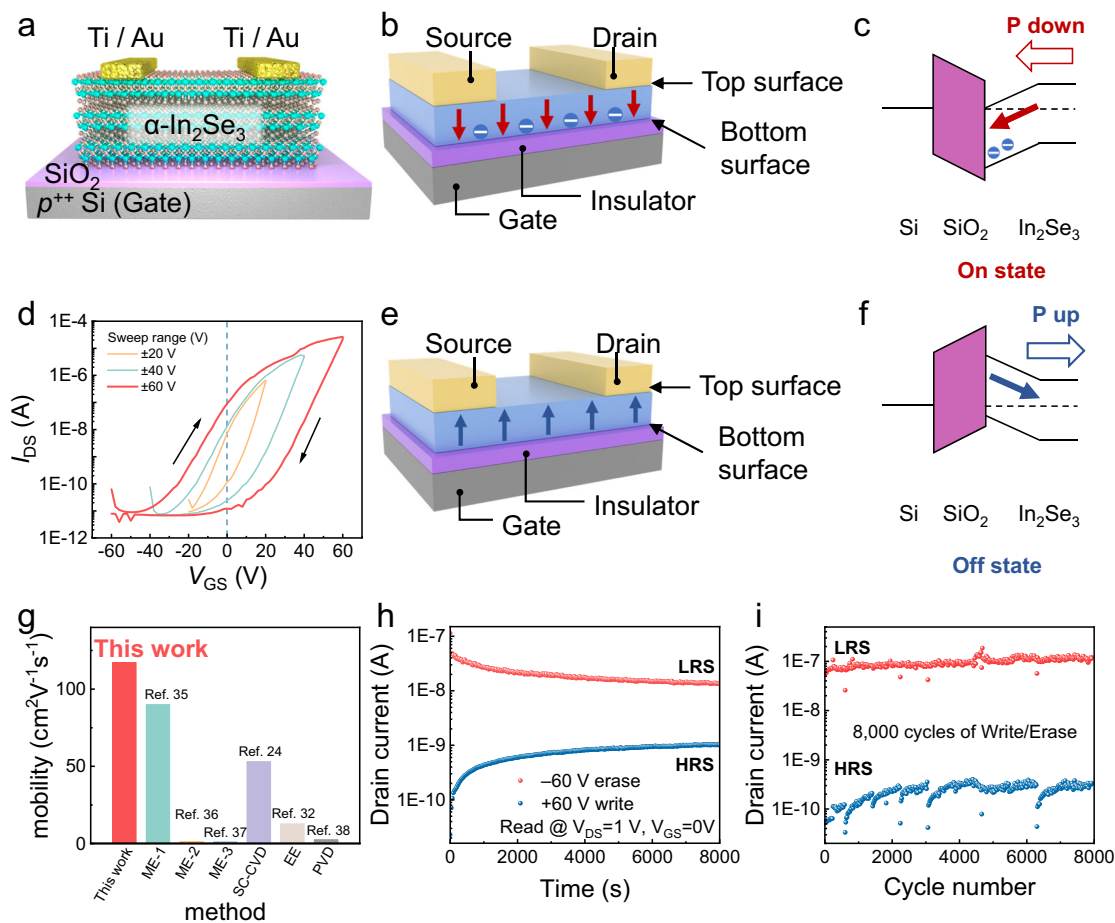
Fig. 4 | Mechanism and performance of non-volatile ferroelectric field-effect transistors (Fe-FETs) device of α-In$_2$Se$_3$. a Schematic of the memory device of α-In$_2$Se$_3$. **b, e** Schematic of Fe-FET at P-down (**b**) and P-up (**e**) state. **c, f** Band bending of P-down (**c**) and P-up (**f**) state. The arrows indicate the direction of ferroelectric polarization. The solid lines and dashed lines represent the energy bands and the Fermi level, respectively. **d** Hysteresis in transfer curve of α-In$_2$Se$_3$ during double sweeping with various gate-source voltage (V_{GS}) sweep ranges. I_{DS} represents drain-source current. **g** Mobility of α-In$_2$Se$_3$ prepared by different strategies (ME mechanical exfoliation, SC-CVD space-confined chemical vapor deposition, EE electrochemical exfoliation, PVD physical vapor deposition)[24,32,35–38]. **h** Retention measurement of α-In$_2$Se$_3$ device by V_{GS} control. **i** Endurance of the α-In$_2$Se$_3$ device after 8000 write/erase cycles, showing no obvious degradation of high resistance state (HRS) and low resistance state (LRS).

Furthermore, the thickness of as-grown film can be controlled by the growth time (see details in Supplementary Fig. 23). The ferroelectricity of α-In$_2$Se$_3$ originates from the atomic position change for the mid-layer Se atoms within Se-In-Se-In-Se quintuple layers (Supplementary Fig. 24). To verify the ferroelectric behavior of α-In$_2$Se$_3$, the as-grown film was transferred onto conducting Pt/Si substrate. Phase hysteresis loop characterized by piezo-response force microscopy (PFM) measurements proves robust room-temperature ferroelectricity (Supplementary Fig. 25).

Electrical device performance testing

We explore the FET performance for α-In$_2$Se$_3$ flakes with the thickness of 13.1 nm as the channel materials. Fig 4a shows the device configuration, which contains two electrodes and back gate (p^{++} Si). As a ferroelectric semiconductor, α-In$_2$Se$_3$ hosts both n-type mobile charges and polarized bound charges. When α-In$_2$Se$_3$ is at the polarization-down (P-down) state which is shown in Fig. 4b, the positive polarized bound charges are distributed at bottom surface (BS). Considering the high effective oxide thickness (EOT ~ 285 nm) of the dielectric used in our device, the gate-induced electric field is not strong enough to penetrate the polarization of α-In$_2$Se$_3$ to the top surface (TP). Thus, only partial switching of polarization occurs near the BS. As a result, built-in electric field will induce the band bending, which accumulates electrons, leading to the low-resistance state (LRS, "On state"), as

shown in Fig. 4c. On the contrary, when α-In$_2$Se$_3$ is at the polarization-up (P-up) state (Fig. 4e), the built-in electric field and band bending are along opposite directions compared with those in P-down case, the mobile electrons at BS are depleted (Fig. 4f), resulting in high-resistance state (HRS, "Off state"). Large clockwise transfer characteristic loops have been observed under varying bidirectional scanning voltages (Fig. 4d), where the source-drain voltage (V_{DS}) is 1 V. The hysteresis window is as large as ~39.8 V when the sweep range is ±60 V, and the on/off ratio is beyond 10^6. Compared to α-In$_2$Se$_3$ flakes prepared by other methods, our sample has a high mobility of 117.2 cm^{2}V^{-1}s^{-1} in the reverse sweep (Fig. 4g). Therefore, we conclude that single crystal samples obtained in our methods with high quality can be fabricated as high-performance computing devices with low energy consumption.

Due to the single-crystalline nature of the channels without grain boundaries, the built-in electric field is less affected by the defect charges and structural distortion, leading to a long retention time and improved endurance of NVM. The FET based on single crystal α-In$_2$Se$_3$ shows a long retention time of over 8000 s (Fig. 4h). The endurance measurement was also conducted with write/erase voltages at ±60 V. The device exhibits remarkable cycling stability, with over 8,000 write/erase cycles recorded (Fig. 4i). When the V_{GS} is 0 V during the test process, the electric current at the LRS maintains a value greater by two orders of magnitude than that at the HRS. The long retention time
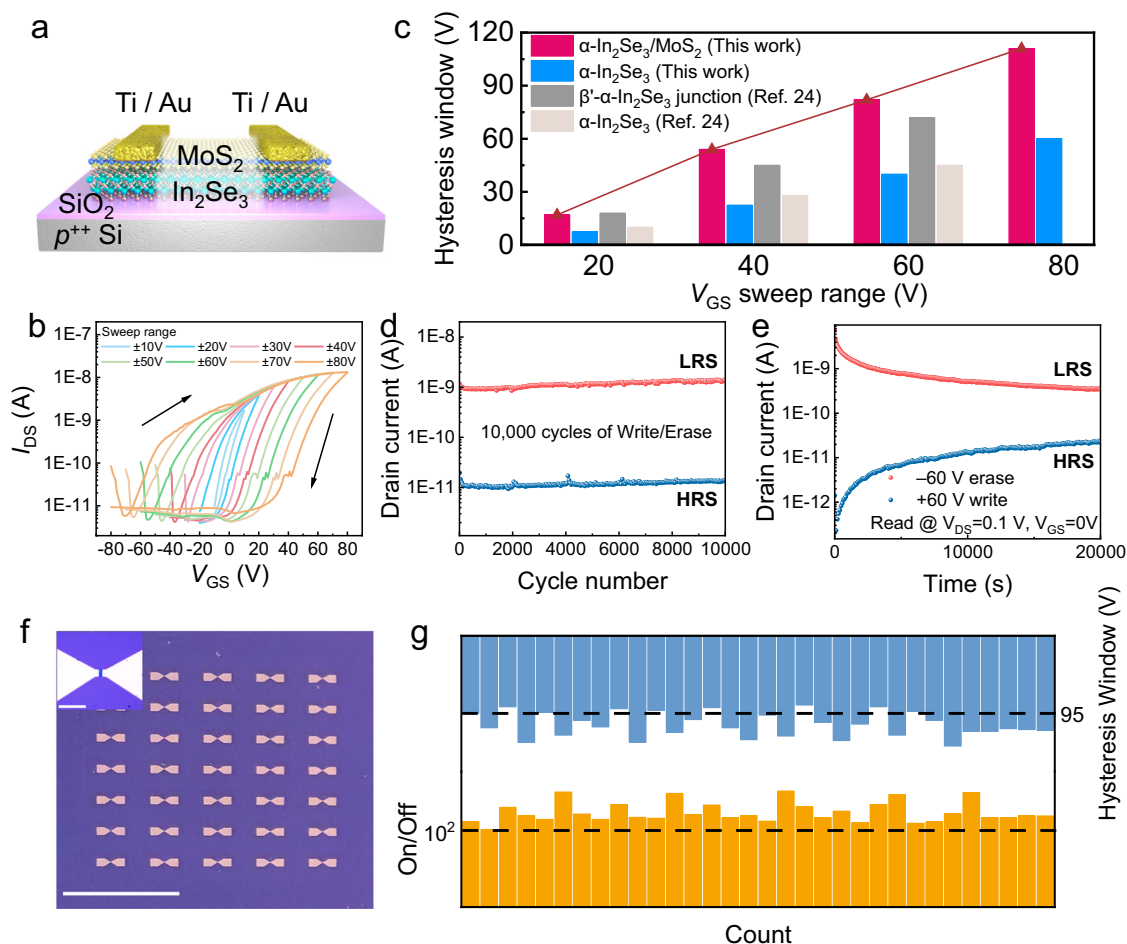
Fig. 5 | Fabrication and device performance of heterostructure of 1L-α-In₂Se₃/1L-MoS₂. a Schematic of the heterostructure device. **b** Hysteresis transfer characteristic loops of α-In₂Se₃/MoS₂ device during double sweeping with various V_{GS} sweep ranges. **c** Hysteresis windows plotted with various V_{GS} sweep ranges of our α-In₂Se₃/MoS₂ heterostructure, as-grown α-In₂Se₃, β'-α-In₂Se₃ heterophase junctions[24] and α-In₂Se₃[24] devices. **d** Robust endurance of the α-In₂Se₃ device after 10,000 write/erase cycles, without the degradation of HRS and LRS. **e** Retention measurement on the heterostructure non-volatile memory (NVM) device by gate voltage control. **f** Optical image of a back-gated FET array of In₂Se₃/MoS₂ fabricated on an Si/SiO₂ substrate. Scale bar: 5 mm. Inset scale bar: 80 μm. **g** Statistical bar graph of hysteresis window and on/off ratio. Yellow and blue bar denote on/off ratio and hysteresis window. The horizontal dashed lines represent a hysteresis window of 95 V (up) and an on/off ratio of 10² (down), respectively.

and endurance measurement demonstrate an reliable NVM performance, comparable to the best results reported on α-In₂Se₃[24]. Furthermore, transfer curve (Supplementary Fig. 26) at various speeds of V_{GS} shows a similar hysteresis window, indicating low doping and defect levels[24]. All the tests above suggest that as-grown α-In₂Se₃ has a considerably high crystalline quality and can be a good candidate for high-performance computing and memory devices.

Furthermore, we fabricated a vertical heterostructure composed of monolayer α-In₂Se₃ (~0.9 nm) and monolayer MoS₂ (~0.8 nm) to explore the performance Fe-FET (Fig. 5a). In this device, the ferroelectric monolayer α-In₂Se₃ acts as a part of gate insulator to tune the electronic properties of n-type MoS₂ as channels, due to the large band gap of ~2.8 eV for monolayer α-In₂Se₃ (see Supplementary Figs. 27 and 28 for analysis). It is believed that the heterostructure formed in the 2D limit is not only benefit to improve the integration, but also for the low-power consumption of emerging devices. The transfer characteristic loops under varying bidirectional scanning voltages show a similar clockwise hysteresis with pure α-In₂Se₃ FET. The clockwise hysteresis is due to the formation of a trap layer at the In₂Se₃/MoS₂ interface, which modulates the carriers in the MoS₂ channel. When α-In₂Se₃ is in P-up (P-down) state, electrons (holes) are trapped in the interface (Supplementary Fig. 29). The accumulated charges in α-In₂Se₃/MoS₂ interface trap layer tune the on/off of MoS₂,

resulting in clockwise hysteresis. The hysteresis window reaches ~100 V when the sweep range is ±80 V and V_{DS} is 0.1 V (Fig. 5b). Compared with as-grown α-In₂Se₃, β'-α-In₂Se₃ heterophase junctions[24] and α-In₂Se₃ grown by SC-CVD[24], the device within 1L-α-In₂Se₃/1L-MoS₂ presents much-larger hysteresis window (Fig. 5c), indicating a better memory performance[25]. The monolayer MoS₂ in this configuration forms capacitors with gate electrode and promote a more uniform polarization of monolayer α-In₂Se₃, contributing to large hysteresis windows, which also demonstrates that α-In₂Se₃ maintains excellent ferroelectricity even at its thinnest limit.

Retention and endurance tests were performed to characterize the memory performance of our Fe-FET by gate voltage control. In α-In₂Se₃ with an the thickness of monolayer, charges trapped at both the upper and lower interfaces create a stronger built-in electric field. This is beneficial to maintain ferroelectric polarization and thus improve memory performance. The α-In₂Se₃/MoS₂ device demonstrates remarkable cycling stability over 10,000 write/erase cycles (Fig. 5d), showing negligible HRS and LRS degradation. The source-drain current at LRS maintains a value greater by two orders of magnitude than that at HRS. The device also displays an exceptional retention time of over 20,000 s (Fig. 5e) with write/erase voltage of ±80 V. After 20,000 s of continuous work, the heterostructure device is still able to maintain a stable non-volatile. The device composed of two monolayer

2D materials shows potential for high-integration non-volatile memory devices and in-memory computing.

To assess the uniformity of the prepared monolayer In_2Se_3 films, we transfer In_2Se_3 films and MoS_2 grown by CVD to construct device arrays of In_2Se_3/MoS_2 heterostructures on Si/SiO_2 (Fig. 5f). Figure 5g and Supplementary Fig. 30 plot the transfer curves, on/off ratios, and hysteresis window of 32 FETs with a 10 μm channel length. Each transfer curve demonstrated consistently excellent performance (Supplementary Fig. 30). The on/off ratio and hysteresis window are extracted from these transfer curves. As illustrated in the Fig. 5g, the on/off ratio for each device exceeds 10^2, and the hysteresis window size for most devices surpasses 95 V. Notably, the MoS_2 used in this study is synthesized using the NaCl-assisted CVD method. Despite inherent variations among different MoS_2 flakes, which could potentially impact the uniformity analysis of the In_2Se_3 thin film, our devices consistently exhibited high performance. This robust performance highlights the uniformity and reliability of the monolayer In_2Se_3 thin film.

In summary, we have achieved single-crystal film growth of monolayer 2D materials on fluor-phlogopite. The 3-fold rotational symmetry of cleavage surface atoms in fluor-phlogopite guarantees the orientation of materials with 3-fold symmetric lattice. In the epitaxial growth, the α-In_2Se_3 flakes present a single orientation, and finally splice to form an inch-scale single-crystal film. The semi-closed environment, small source-substrate distance, and the liquid intermediate state provide a quasi-equilibrium growth environment without disturbance, exhibiting high repeatability in growing single-crystal film and tolerance to varying conditions. As-grown samples possess excellent crystallinity, low doping levels, and high mobility. The memory transistor devices based on these films exhibit long retention time, and stable cycling endurance, which is comparable to mechanically exfoliated samples. Moreover, the excellent performance of 1L-In_2Se_3/1L-MoS_2 devices shows the potential for integration applications of as-grown films. Our controllable synthesis strategies for large-area α-In_2Se_3 films provide a platform for future ferroelectric electronics and memory devices.

Methods

Quasi-equilibrium growth of α-In_2Se_3
The α-In_2Se_3 films were grown in a tube furnace. α-In_2Se_3 powders were mixed with KI powders by the mass ratio of (30–90):1 as the precursors. 50sccm–1000sccm high-purity Ar mixed with 5% H_2 was used as environment atmosphere. Freshly exfoliated fluor-phlogopite ($KMg_3AlSi_3O_{10}F_2$) with a size of 1 cm × 1 cm or 3 cm × 3 cm was used as the growth substrate. A cubic quartz boat with a size of 0.9 cm × 0.9 cm × 0.7 cm or 2.9 cm × 2.9 cm × 0.5 cm was used for loading the precursor powders and fluor-phlogopite substrates. The distance between precursors and substrate is less than 1 mm. Before heating, the tube is scrubbed by H_2/Ar mixed gas or argon to remove the oxygen for 5 min. The growth temperature was within 650–850 °C and maintained for 3–30 min. The reaction was performed under atmospheric pressure.

Transfer method of α-In_2Se_3 films
α-In_2Se_3 films were transferred from fluor-phlogopite to SiO_2/Si or TEM grids by wet-transfer method. First, the poly (methyl methacrylate) (PMMA) was spin-coated onto fluor-phlogopite at 3000 rpm for 60 s and then heated at 150 °C for 1 min. Second, the PMMA was spin-coated again at 3000 rpm for 30 s and heated at 100 °C for 10 min. Subsequently, PMMA with α-In_2Se_3 film was stripped off in water and covered SiO_2/Si or TEM grids. Then, the PMMA films covered SiO_2/Si or TEM grids were dried naturally, and dropped a few drops of acetone before another heat treatment at 100 °C for 5 min. Finally, PMMA was removed by immersing in acetone and isopropanol successively.

Materials characterization
The morphologies, Raman spectra, and thickness of the samples were acquired by optical microscopy (Olympus CX41), Raman spectroscopy (iHR 500 with 532 nm laser excitation), and AFM (Bruker Icon), respectively. HRTEM and EDS were performed using a JEM-2100F TEM operating at 200 kV.

The samples used for XPS and AES were transferred onto a SiO_2/Si substrate to eliminate the effects of the K element in fluor-phlogopite.

PFM measurements
The α-In_2Se_3 film was transferred onto a platinum substrate. A voltage was applied to the conductive probe by PFM to change the local polarization direction. The α-In_2Se_3 samples were transferred onto a platinum substrate without any coating deposited on the sample surface. A voltage was applied to the conductive probe by PFM to change the local polarization direction. An SCM-PIT model tip was used. The swept voltage range was set to ±10 V. The drive frequency and drive amplitude were set to 67 kHz and 9000 mV, respectively.

Device fabrication and FET measurements
α-In_2Se_3 films were transferred onto SiO_2(285 nm)/Si substrate by wet-transfer method. Laser direct writing lithography and e-beam evaporation of Ti/Au (10 nm/40 nm) were used to fabricate two terminal field effect transistors. All the devices were tested by Keithley 4200 semiconductor analyzer in a vacuum to avoid attacks from oxygen and moisture under a dark environment.

Extraction of electrical parameters
The field-effect mobility (μ) was computed from the equation $\mu = \frac{dI_{DS}}{dV_{GS}} \times \frac{L}{WC_iV_{DS}}$, where $\frac{dI_{DS}}{dV_{GS}}$ is the maximum transconductance; L and W are the channel length and width, respectively; C_i is the capacitance of the 285-nm-thick SiO_2 (1.15×10^{-4} F m^{-2}); and V_{DS} is the drain voltage.

The maximum hysteresis window ($V_{hysteresis}$) was calculated from the equation $V_{hysteresis} = V_{reverse} - V_{forward}$, under the same drain current.

Growth and transfer of monolayer MoS_2 flakes
In a typical CVD process, 1 mg MoO_3 and SiO_2/Si substrate were loaded into the quartz boat and placed in downstream zone 2 (T_2 = 750 °C; heating rate, 30 °C min^{-1}). The MoO_3 powder was evenly dispersed and the SiO_2/Si substrate was placed above the powder at a 5 mm distance. Then, 100 mg of S powder was placed in upstream zone 1 (T_1 = 180 °C; heating rate, 10 °C min^{-1}). 80sccm Ar was used as carrier gas. The reaction process was maintained for 5 min. After growth, the furnace was naturally cooled to room temperature.

MoS_2 flakes were transferred by the wet-transfer method. The samples were spin-coated with PMMA and then etched with 3% KOH solution. Afterward, the peeled-off PMMA/sample layer was rinsed with deionized water and placed on a substrate with α-In_2Se_3 film. Finally, PMMA was washed off with acetone and isopropanol.

DFT calculation
All density functional theory (DFT) calculations were carried out by Vienna Ab Initio Simulation Package (VASP)[26,27]. The generalized gradient approximation in the Perdew-Burke-Ernzerhof functional was applied[28], and the cutoff energy of the plane wave set as 300 eV. The convergence criterion for energy and force were set to 1e^{-5} eV and 1e^{-4} eV/Å. Periodic boundary conditions were applied in the in-plane directions of layer, while adding a vacuum layer with a thickness >10 Å in the out-of-plane direction. The stable structure of the α-In_2Se_3 flake with 3-fold symmetry placed on the substrate is attained through energy optimization, where the substrate is a single layer cut from pristine fluor-phlogopite. Considering the large number of atoms in the structure, we only retained the atoms that interact with α-In_2Se_3 flake of the monolayer fluor-phlogopite substrate in the binding

energy calculation. The binding energy is determined by subtracting the energy of individual components from the energy of the entire structure. The $1 \times 1 \times 1$ grid was used to calculate the single-point energy of structures.

Data availability

Relevant data supporting the key findings of this study are available within the article and the Supplementary Information file. All raw data generated during the current study are available from the corresponding authors upon request.

References

1. Radisavljevic, B., Radenovic, A., Brivio, J., Giacometti, V. & Kis, A. Single-layer MoS₂ transistors. *Nat. Nanotechnol.* **6**, 147–150 (2011).
2. Desai, S. B. et al. MoS₂ transistors with 1-nanometer gate lengths. *Science* **354**, 99–102 (2016).
3. Bandurin, D. A. et al. High electron mobility, quantum Hall effect and anomalous optical response in atomically thin InSe. *Nat. Nanotechnol.* **12**, 223–227 (2017).
4. Manzeli, S., Ovchinnikov, D., Pasquier, D., Yazyev, O. V. & Kis, A. 2D transition metal dichalcogenides. *Nat. Rev. Mater.* **2**, 1–15 (2017).
5. Liu, C. et al. Two-dimensional materials for next-generation computing technologies. *Nat. Nanotechnol.* **15**, 545–557 (2020).
6. Fiori, G. et al. Electronics based on two-dimensional materials. *Nat. Nanotechnol.* **9**, 768–779 (2014).
7. Greuter, F. & Blatter, G. Electrical properties of grain boundaries in polycrystalline compound semiconductors. *Semicond. Sci. Technol.* **5**, 111 (1990).
8. Chen, T.-A. et al. Wafer-scale single-crystal hexagonal boron nitride monolayers on Cu (111). *Nature* **579**, 219–223 (2020).
9. Xu, X. et al. Seeded 2D epitaxy of large-area single-crystal films of the van der Waals semiconductor 2H MoTe₂. *Science* **372**, 195–200 (2021).
10. Yang, P. et al. Epitaxial growth of inch-scale single-crystal transition metal dichalcogenides through the patching of unidirectionally orientated ribbons. *Nat. Commun.* **13**, 3238 (2022).
11. Liu, L. et al. Uniform nucleation and epitaxy of bilayer molybdenum disulfide on sapphire. *Nature* **605**, 69–75 (2022).
12. Li, T. et al. Epitaxial growth of wafer-scale molybdenum disulfide semiconductor single crystals on sapphire. *Nat. Nanotechnol.* **16**, 1201–1207 (2021).
13. Wang, L. et al. A scanning microwave impedance microscopy study of α-In₂Se₃ ferroelectric semiconductor. *Adv. Funct. Mater.* https://doi.org/10.1002/adfm.202316583 (2024).
14. Wang, X. et al. Van der Waals engineering of ferroelectric heterostructures for long-retention memory. *Nat. Commun.* **12**, 1109 (2021).
15. Ding, W. et al. Prediction of intrinsic two-dimensional ferroelectrics in In₂Se₃ and other III₂-VI₃ van der Waals materials. *Nat. Commun.* **8**, 14956 (2017).
16. Si, M. et al. A ferroelectric semiconductor field-effect transistor. *Nat. Electron.* **2**, 580–586 (2019).
17. Quhe, R. et al. Asymmetric conducting route and potential redistribution determine the polarization-dependent conductivity in layered ferroelectrics. *Nat. Nanotechnol.* **19**, 173–180 (2024).
18. Liu, K. et al. An optoelectronic synapse based on α-In₂Se₃ with controllable temporal dynamics for multimode and multiscale reservoir computing. *Nat. Electron.* **5**, 761–773 (2022).
19. Christenson, H. K. & Thomson, N. H. The nature of the air-cleaved mica surface. *Surf. Sci. Rep.* **71**, 367–390 (2016).
20. Zhang, P. et al. Flux-assisted growth of atomically thin materials. *Nat. Synth.* **1**, 864–872 (2022).
21. Li, S. et al. Vapour-liquid-solid growth of monolayer MoS₂ nanoribbons. *Nat. Mater.* **17**, 535–542 (2018).
22. Dong, J., Zhang, L., Dai, X. & Ding, F. The epitaxy of 2D materials growth. *Nat. Commun.* **11**, 5862 (2020).
23. Xu, C. et al. Two-dimensional antiferroelectricity in nanostripe-ordered In₂Se₃. *Phys. Rev. Lett.* **125**, 047601 (2020).
24. Han, W. et al. Phase-controllable large-area two-dimensional In₂Se₃ and ferroelectric heterophase junction. *Nat. Nanotechnol.* **18**, 55–63 (2023).
25. Hong, A. J. et al. Graphene flash memory. *ACS Nano* **5**, 7812–7817 (2011).
26. Kresse, G. & Furthmüller, J. Efficiency of ab-initio total energy calculations for metals and semiconductors using a plane-wave basis set. *Comput. Mater. Sci.* **6**, 15–50 (1996).
27. Kresse, G. & Furthmüller, J. Efficient iterative schemes for ab initio total-energy calculations using a plane-wave basis set. *Phys. Rev. B* **54**, 11169–11186 (1996).
28. Perdew, J. P., Burke, K. & Ernzerhof, M. Generalized gradient approximation made simple. *Phys. Rev. Lett.* **77**, 3865–3868 (1996).
29. Lin, M. et al. Controlled growth of atomically thin In₂Se₃ flakes by van der Waals epitaxy. *J. Am. Chem. Soc.* **135**, 13274–13277 (2013).
30. Rashid, R. et al. Shape-control growth of 2D-In₂Se₃ with out-of-plane ferroelectricity by chemical vapor deposition. *Nanoscale* **12**, 20189–20201 (2020).
31. Cui, C. et al. Intercorrelated in-plane and out-of-plane ferroelectricity in ultrathin two-dimensional layered semiconductor In₂Se₃. *Nano lett.* **18**, 1253–1258 (2018).
32. Gao, X. et al. Thin-film transistors from electrochemically exfoliated In₂Se₃ nanosheets. *Micromachines* **13**, 956 (2022).
33. Sun, X. et al. Alpha-phase indium selenide saturable absorber for a femtosecond all-solid-state laser. *Opt. Lett.* **44**, 699–702 (2019).
34. Poh, S. M. et al. Molecular-beam epitaxy of two-dimensional In₂Se₃ and its giant electroresistance switching in ferroresistive memory junction. *Nano Lett.* **18**, 6340–6346 (2018).
35. Wang, L. et al. Exploring ferroelectric switching in α-In₂Se₃ for neuromorphic computing. *Adv. Funct. Mater.* **30**, 2004609 (2020).
36. Feng, W. et al. Phase-engineering-driven enhanced electronic and optoelectronic performance of multilayer In₂Se₃ nanosheets. *ACS Appl. Mater. Interfaces* **10**, 27584–27588 (2018).
37. Wang, S. et al. Strong anisotropic two-dimensional In₂Se₃ for light intensity and polarization dual-mode high-performance detection. *ACS Appl. Mater. Interfaces* **15**, 3357–3364 (2023).
38. Zhou, J. et al. Controlled synthesis of high-quality monolayered α-In₂Se₃ via physical vapor deposition. *Nano Lett.* **15**, 6400–6405 (2015).

Acknowledgements

Author contributions

Y.G. and P.Z. supervised and led the research project. K.S. carried out the synthesis with assistance from F.D., Y.Z., X.W., and B.L.; Y.Z. and F.D. performed the density functional theory calculations. P.T. contributed to the analysis of the device mechanism. Q.H. carried out the TEM characterizations. K.S. carried out Raman and SEM characterizations. K.S. carried out the device fabrication and testing with assistance from J.W.

and Y.W.; K.S., Z.H., and A.C. carried out the atomic force microscopy and piezo-response force microscopy characterizations. All the authors contributed to discussions.

Competing interests

The authors declare no competing interests.

Additional information

Correspondence and requests for materials should be addressed to Peng Zhang, Peizhe Tang, Feng Ding or Yongji Gong.

Reprints and permissions information is available at http://www.nature.com/reprints

Publisher's note Springer Nature remains neutral with regard to jurisdictional claims in published maps and institutional affiliations.